Non-invasive damage detection in beams using marker extraction and wavelets

Yi-Zhe Song[1]**, Chris R. Bowen**[2]**, H Alicia Kim**[2]**, Aydin Nassehi**[2]**, Julian Padget**[1]**, Nick Gathercole**[2] **and Andrew Dent**[2]

[1] Department of Computer Science, University of Bath, Claverton Down, Bath, BA2 7AY, UK

[2] Department of Mechanical Engineering, University of Bath, Claverton Down, Bath, BA2 7AY, UK

E-mail: `c.r.bowen@bath.ac.uk`

Abstract. For structural health monitoring applications there is a need for simple and contact-less methods of Non-Destructive Evaluation (NDE). A number of damage detection techniques have been developed, such as frequency shift, generalized fractal dimension and wavelet transforms with the aim to identify, locate and determine the severity of damage in a material or structure. These techniques are often tailored for factors such as (i) type of material, (ii) damage pattern (crack, delamination), and (iii) the nature of any input signals (space and time). This paper describes and evaluates a wavelet-based damage detection framework that locates damage on cantilevered beams via NDE using computer vision technologies. The novelty of the approach is the use of computer vision algorithms for the contact-less acquisition of modal shapes. Using the proposed method, the modal shapes of cantilever beams are reconstructed by extracting markers using sub-pixel Hough Transforms from images captured using conventional slow motion cameras. The extracted modal shapes are then used as an input for wavelet transform damage detection, exploiting both discrete and continuous variants. The experimental results are verified and compared against finite element analysis. The methodology enables a non-invasive damage detection system that avoids the need for expensive equipment or the attachment of sensors to the structure. Two types of damage are investigated in our experiments: (i) defects induced by removing material to reduce the stiffness of a steel beam and (ii) delaminations in a $(0/90/0/90/0)_s$ composite laminate. Results show successful detection of notch depths of 5%, 28% and 50% for the steel beam and of 30mm delaminations in central and outer layers for the composite laminate.

Keywords: Non-Destructive Evaluation (NDE), Wavelet Transform, Hough Transform, Image Processing, Visual Tracking

1. INTRODUCTION AND RELATED WORK

Structural Health Monitoring (SHM) has been an active research area in recent decades and is considered to be of major importance due to its potential benefits in terms of economics, reliability and safety. The ability to detect damage in a structure is a key component of any modern SHM system and Non-Destructive Evaluation (NDE) is an important element of any such system because of its convenient and non-invasive nature.

NDE methods based on modal parameters and shapes obtained using vibration-based testing are highly effective [1, 2]. The cornerstone of vibration-based damage detection lies in the mapping between modal parameters and changes in the physical properties of a structure. Essentially, such mapping transfers the feature space in which damage detection algorithms operate from that of mass, damping and stiffness to one constructed from modal frequencies, modal damping and modal shapes. Damage detection algorithms are often categorised by the type of modal properties they work with. One of the first comprehensive reviews of vibration-based damage detection was by Doebling et. al. [3]. The authors provide a thorough review of structural damage detection techniques prior to 1996 and categorised the methods based on the type of modal property used as an input, followed by [4, 5, 1]. Recently, Fan and Qiao [6] offered an in-depth survey of vibration-based damage identification methods. A categorisation method similar to Doebling et. al. [3] was followed, with particular emphasis on advances in damage detection algorithms through the means of modern signal processing techniques, such as Wavelet Transforms (WT). Since the introduction of WT for damage detection by Hou et. al. [7] and Okafor and Dutta [8], WT-based damage detection techniques have generally been shown to outperform others in terms of their ability to detect damage robustly and its location [9, 2], though conventional techniques such as frequency shift still remains a popular choice under certain scenarios [10].

Modal shapes, often obtained from experimental modal analysis, are widely used as an input for WT-based damage detection algorithms. Acquiring modal shapes in practice usually involves installing a large number of sensors which is not always straightforward or practical. This not only makes the installation process labour-intensive, but can also influence structural/vibrational properties. For example, a common experimental modal analysis uses an array of accelerometers mounted on a structure to compute Frequency Response Functions (FRFs), which collectively form modal shapes via various forms of curve fitting. Such approaches have two common drawbacks: (i) adding sensors can add undesirable damping effects on the structure; altering its modal properties [11]; (ii) the total number of sensors deployable are largely limited by the physical form of the accelerometers, this places a bottleneck on the spatial resolution of the acquired modal shapes, which makes damage localisation less accurate [2]. In addition, if the accelerometers are not wireless, a significant amount of cabling must also be be laid throughout the structure.

To overcome these disadvantages, contact-less methods to extract modal shapes also exist, such as Laser Doppler Vibrometers (LDV) [8], which are able to measure

the motion of a structure. However such systems are expensive and cannot readily be deployed within a structure [12]. Wang et. al. [13] recently used a laser profile sensor to measure the static profiles of delaminated aluminium and steel beams. Spatial wavelet transforms were used to detect delamination damage. One outcome of their work was the identification of the need to move away from laser displacement sensors and also examine composite/laminate structures. This paper aims to address these needs.

We therefore propose a novel methodology for structural damage detection which encapsulates a modal shape reconstruction algorithm based on computer vision techniques and a wavelet-based damage detection algorithm tailored to work with such modal shapes. This makes use of the latest developments in vision technology, taking advantage of: (i) recent advances in the areas of saliency detection [14, 15] and tracking [16] and (ii) the availability of cost-effective camera sensor nodes.

Other researchers have also advocated the utilization of cameras for damage detection, specifically Patsias and Staszewskiy [12] and Shi et. al. [17]. Patsias and Staszewskiy [12] extracted the edges of a cantilevered beam using a standard wavelet-based algorithm. Discretely stored edge profiles were treated as modal shapes and the authors used a different wavelet-based approach to detect damage. In contrast, Shi et. al. [17] report on a method very similar to that which we present, in which they obtain modal shapes via standard edge detection techniques using commercial software and the modal shapes are represented at discrete pixel locations, where local jaggedness of edges is acquired from the image representation. The technique was demonstrated on a damaged aluminium cantilever beam. We specifically address shortcomings identified in [17] by introducing a more accurate modal shape construction technique and better feature detection, leading to a reduction in false damage reports. In addition, we evaluate the technique on a composite laminate.

In this work, rather than attaching accelerometers/strain sensors to a structure or using laser positioning systems, we simply paint markers on the structure, so that their position can be determined using a sub-pixel accuracy marker extraction algorithm. The markers can be regarded as zero-mass 'virtual sensors' from which modal shapes are reconstructed. With the help of these visual markers, which can then be successfully utilized in a WT-based damage detection algorithm. Such a setup has two important benefits: first, managing sensors becomes easy since they are freely available and easily (re-)deployable; second, a single camera node can read many markers and efficiently transmit the acquired data across a network.

In summary, this paper will:

(i) Demonstrate how computer vision technology can be utilized on structural beams as a contact-less and low-cost technique for the acquisition of modal properties for damage detection algorithms.

(ii) Investigate how the acquired modal shapes can be used in practical damage detection tasks, where both the discrete and continuous versions of the wavelet transform are applied, taking advantage of their robustness to noise – an essential
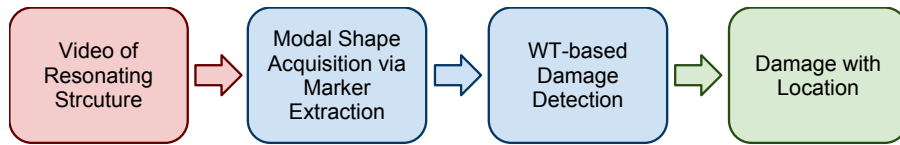
Figure 1. A system diagram of the proposed damaged detection process

property for practical damage detection.

(iii) Compare two different damaged materials (steel and Carbon Fibre Reinforced Plastic (CFRP)), based on both experimental and finite element analysis data, to evaluate the performance of the damage detection system.

2. METHOD

The proposed damage detection concept has two phases: after taking a video of a structure resonating under one of its modal frequencies, we first extract markers from each frame and use standard curve-fitting techniques to reconstruct the modal shape. The second phase uses specific WT-based damage detection algorithms to detect and locate damage on the structure. This process is illustrated in Figure 1.

2.1. Marker-Based Modal Shape Acquisition

There are two key design considerations in the marker extraction stage for damage detection: accuracy and efficiency. This is achieved by extending the Hough Transform (HT) to sub-pixel accuracy and proposing marker registration via a tracking-by-correspondence framework. Accurate marker positions yield more accurate modal shapes which in turn enable more robust detection; whereas, efficiency not only increases applicability of the damage detection framework, but also plays an important part in real-time monitoring applications.

Classical HT [18] and its variants generally locate features having pure geometric shapes, i.e, lines, circles and squares. Because of the geometric nature of Hough features, HT is more tolerant to discontinuities and more robust to noise than markerless feature extraction techniques [18]. Although modern computer vision algorithms can detect points of interest in a range of applications such as 3D reconstruction and object recognition, they are still prone to the influence of outliers and post-processing is commonly required. However, combining markers and HT can lead to more robust detection. The HT can also be computed very efficiently, in real-time [19].

For our purposes, we use the Circular Hough Transform (CHT) to detect the position of markers deployed on a structure. CHT determines the radius, R, of a circle by locating points that lie on its perimeter. The idea behind CHT is that a point, (x, y), in image space corresponds to a circle of radius R centred at (a, b) in the parameter space. The parametric form of a circle is often used:
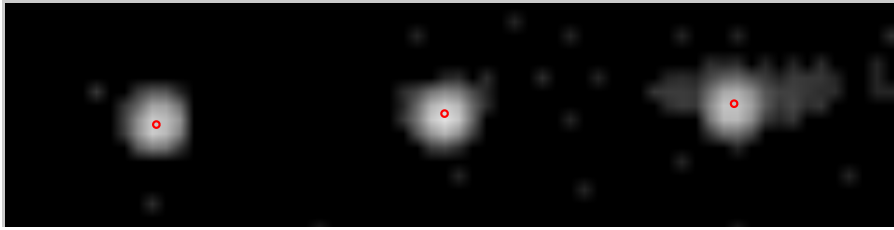
$$x = a + R\cos(\theta) \tag{1}$$
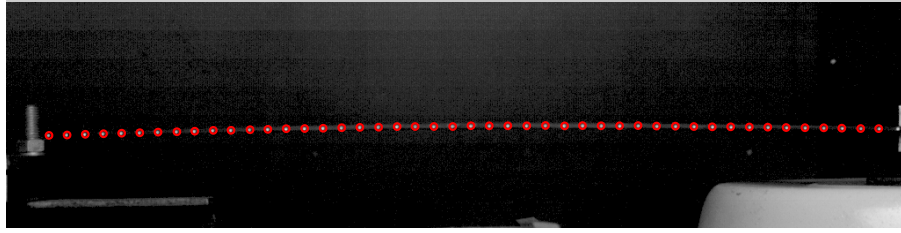
(a) marker extraction on a cantilever beam clamped at right hand side
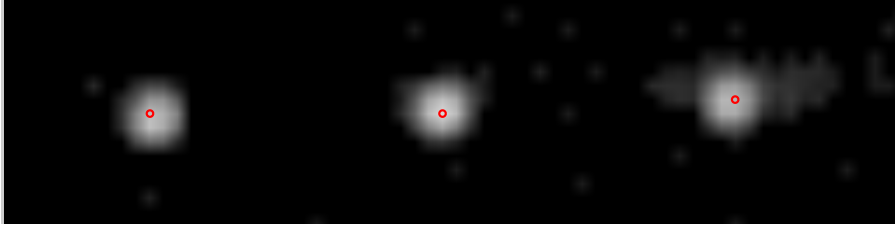
(b) standard HT result, close-up of three markers

(c) sub-pixel HT result, close-up of three markers

Figure 2. Marker extraction result (Beam Material: CFRP, Beam Length: 463mm, Mode Number: 2, Marker spacing is 10mm)

$$y = b + R\sin(\theta) \tag{2}$$

where R is the unknown radius and (a, b) is the centre. θ determines the location of a point, (x, y), on the circle's perimeter. The triplet (a, b, R) constitutes the Hough parameter space of an image and a CHT algorithm searches such a space to locate circles. A voting procedure is then carried out to build an accumulation array, A, where local maxima corresponds to circle centres in the image space. A is a two-dimensional accumulator array that has the same size as the input image and each dimension corresponds to quantised values for a and b.

Figure 2(a) shows a series of markers on the edge of a cantilever beam which is fixed at the right hand side of the image. Circle centres detected using standard CHT are often offset from the actual centre, as can be seen in Figure 2(b). This is largely due to the limit in the spatial resolution of images; an inevitable result of the discrete sampling nature of digitised images. However, more accurate localisation of markers makes them more able to deliver modal shapes that can be reliably used to detect damage.

We therefore extend the standard HT algorithm to sub-pixel accuracy to yield more accurate signals. We follow a similar approach to that developed by Lowe [20], but modified to find sub-pixel locations of circle centres. The method works with a

Difference of Gaussians (DoG) scale-space:

$$D(x, y, \sigma) = G(x, y, k_i\sigma) * I(x, y) - G(x, y, k_j\sigma) * I(x, y) \tag{3}$$

where I is a greyscale image (two-dimensional array of pixel intensities), $G(x, y, k_i\sigma)$ is a Gaussian blur kernel centred around point (x, y) of scale k_i ($i < j$ are kernel scale indices and σ is the 'octave' scale) and '$*$' stands for the convolution operation. Here, we use the previously calculated Hough accumulation array, A, as the input image, $I = A$. The true maxima of A are then estimated by interpolating neighbouring pixels of each provisional one and fitting a 3D quadratic function to them. A Taylor expansion (up to the quadratic term) of the DoG scale-space function $D(x, y, \sigma)$ is used for this interpolation, which is given by:

$$D(\mathbf{x}) = D + \frac{\partial D^T}{\partial \mathbf{x}} \mathbf{x} + \frac{1}{2}\mathbf{x}^T\frac{\partial^2 D}{\partial \mathbf{x}^2}\mathbf{x}, \tag{4}$$

where D, $\partial D/\partial \mathbf{x}$ and $\partial^2 D/\partial \mathbf{x}^2$ are evaluated at the provisional centre $\bar{c}$, obtained via the standard HT. The algorithm then seeks to find a suitable offset $\mathbf{x} = (x, y, \sigma)$ that moves $\bar{c}$ to its true centre $\hat{c}$. It follows that its extremum, $\hat{\mathbf{x}}$, can be found by taking the derivative of $D(\mathbf{x})$ with respect to x and setting it to zero, giving

$$\hat{\mathbf{x}} = -\frac{\partial^2 D(\mathbf{x})}{\partial \mathbf{x}^2}^{-1}\frac{\partial D(\mathbf{x})}{\partial \mathbf{x}}. \tag{5}$$

If $\hat{\mathbf{x}}$ is larger than a threshold in any of its three dimensions, the candidate centre is updated to be the new offset point where the same interpolation procedure is performed again; otherwise, the offset is desirable, hence used to find the true maximum using $\hat{c} = \bar{c} + \hat{\mathbf{x}}$.

The results of the above sub-pixel accuracy circle detection algorithm are shown in Figure 2(c). As can be seen, the refined centres offer a better localisation than the classical method (Figure 2(b)). The benefits of sub-pixel HT will be quantified later in the paper.

Using the extracted markers, modal shapes can be constructed using spline fitting. More specifically, given a set of markers, denoted by $P = \{\mathbf{p}_1, \mathbf{p}_2, ..., \mathbf{p}_n\}$ where n is the total number extracted, the corresponding modal shape is generated by fitting a cubic interpolating spline S to P, so that

$$S(\mathbf{r}_i) = \mathbf{p}_i, \mathbf{r}_i \in [0, 1]$$

Figure 3(a) shows a modal shape of a cantilever reconstructed using the above spline interpolation procedure (the modal shape is drawn in yellow with markers in red). A close-up of part of the same modal shape is provided in Figure 3(b). It can be seen that the spline (yellow) reconstructed using the sub-pixel accuracy markers (red) is smooth and rests near the true median axis of the beam (a quantitative experiment shortly follows).

Numerically calculated modal shapes (e.g. via finite element analysis) are perfectly smooth splines, therefore, their experimental realisations should also be smooth. Here 'smooth' stands for the lack of local discontinuities on modal shapes. Local
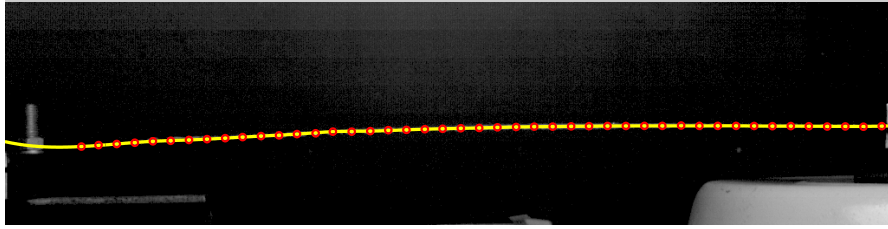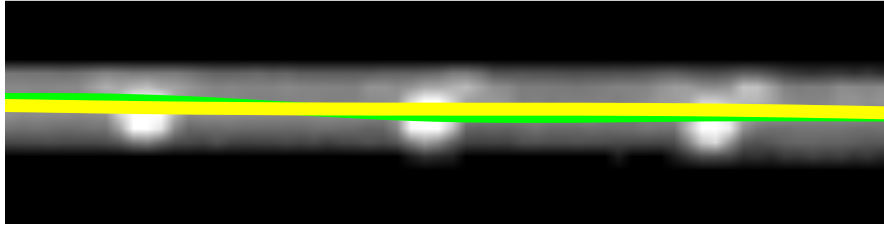
(a) modal shape via spline fitting, beam is clamped at right hand side
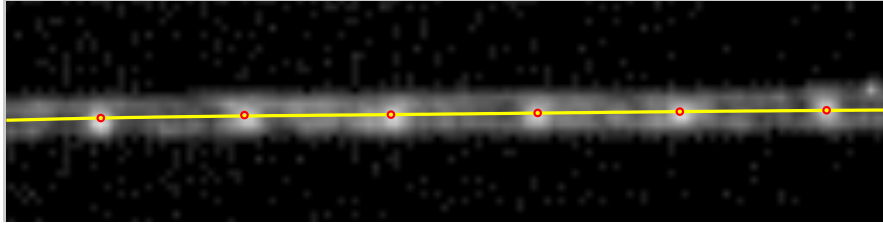
(b) zoomed-in section of the modal shape in (a)

Figure 3. Modal shape reconstruction result (Beam Material: Steel, Beam Length: 463mm, Mode Number: 2, Marker spacing is 10mm)

Figure 4. Modal Shapes: sub-pixel accuracy marker extraction (yellow) vs. standard HT (green), Marker spacing in 10mm

discontinuities often make analysis difficult and can generate false positives in damage detection algorithms [21]. Figure 4 offers a qualitative comparison between modal shapes acquired using our sub-pixel HT(yellow) and using standard pixel level HT(green). It is observed that standard HT yields modal shapes that tend to vary locally, whereas the one reconstructed using our method appears to be smoother.

To quantify the benefit of our sub-pixel HT modal shape construction method, we conduct an experiment using the *mean curvature* of a spline to measure the 'smoothness' of a modal shape, in which, we compare the shapes computed using our sub-pixel HT approach against those obtained via standard HT. For the nine beams used in the damage detection experiment (details appear in Section 3.1), we calculate the mean curvature for each beam resonating under mode 2. The results are summarised in Table 1, where improvements in smoothness over modal shapes obtained via standard HT can be observed for every beam. It is this improvement in overall modal shape smoothness that enables more accurate damage detection results, as Section 3 will later show.

Table 1. Overall Mean Curvatures of All Nine Tested Beams (see Section 3.1)

Beam ID	Overall mean curvature of sub-pixel HT	Overall mean curvature of standard HT	Improvement over standard HT (%)
Steel beam 1	13.45	65.88	79.58%
Steel beam 2	15.42	62.19	75.20%
Steel beam 3	21.32	64.33	66.86%
CFRP beam 1	15.21	66.93	77.27%
CFRP beam 2	21.12	60.09	64.85%
CFRP beam 3	11.45	65.38	82.48%
CFRP beam 4	20.83	59.17	64.79%
CFRP beam 5	13.99	60.90	77.01%
CFRP beam 6	14.49	68.86	78.95%

2.2. Damage Detection using Wavelets

We employed a wavelet-transform (WT) based algorithm to perform damage detection on the modal shapes acquired from the sub-pixel markers. In contrast to Fourier analysis where time (space) information is lost, wavelets are located in time (space) and have 'windows' of variable size. These characteristics allow WT to reveal important information buried within signals that other techniques fail to detect. For example, in the context of damage detection, space information needs to be retained for localisation and damage may only be detected at various scales, rather than just one.

We utilize both the discrete and continuous variants of WT: Continuous WT (CWT) offers accurate localisation of damage; whilst Discrete WT (DWT) delivers noise filtering, which is essential in experimental modal shape acquisition. A CWT of a function $u(t)$ [22] is defined as:

$$CWT(\tau, S) = \frac{1}{\sqrt{|S|}} \int u(t)\psi^*(\frac{t-\tau}{S})\partial t, \tag{6}$$

where τ is the translation parameter, S is the scale parameter, $u(t)$ is the signal to be analysed (t being time/space) and ψ^* is called the 'mother wavelet' — a family of source functions that satisfy the admissibility criterion and the daughter wavelets (those after convolution) are simply the translated and scaled versions of it.

Similar to Rucka et. al. [21], we use "db4" of the Debauchies family of wavelets to perform both DWT and CWT. Other researchers have investigated alternative families of mother wavelets, such as the "gauss" family [9], however, in our studies "db4" gave the better indication of the existence of damage. Specifically, we set $u(t) = \mathbf{s}$ and $S = 1 - 3$ in Equation 6 and damage is located where the CWT coefficients find their global maximum.

In general, CWT provides a measure of similarity between the mother wavelet and

the signal. The calculated wavelet coefficients reflect the strength of the correlation between the signal and the mother wavelet at a given scale. Given a modal shape, **s**, reconstructed using extracted markers, damage can be detected by treating **s** as a time signal and performing a CWT as in Equation 6. Since CWT is naturally sensitive to local discontinuities, it performs best on simulated data where noise is not an issue and the only discontinuity on the modal shape corresponds to the damage location. However, in experimental modal acquisition, measurement noise is inevitable, which can contaminate wavelet responses and make damage assessment inconclusive.

To this end, we also evaluate the modal shapes obtained using DWT [8]. DWT differs from CWT by digitizing the scale parameter, S and the translation parameter, τ from Equation 6, giving:

$$\Psi(t) = \frac{1}{\sqrt{S}}\Psi(\frac{t - p\tau S}{S}),$$ (7)

where the following dyadic sampling is often performed [23]:

$$S = 2^o, \tau = 2^o p$$

where $o, p \in \mathbb{Z}$ with $\mathbb{Z}$ being the set of all positive integers.

An important characteristic of DWT is that of multi-resolution analysis, where signals are broken down into detail and approximation components at each level of the dyadic space. Information that is often not apparent can be reviewed on different levels of a multi-resolution decomposition.

In this work CWT was used after breaking the signal down using DWT. From our damage experiments (Section 3) the third level detail DWT signal gave the best results compared to other levels; a conclusion confirming observations in [21].

3. EXPERIMENTS AND RESULTS

We evaluate the performance of the proposed damage detection methodology using data obtained experimentally and via finite element analysis (FEA). In addition, we also investigate the effectiveness of our methodology on two materials: steel (isotropic) and a CFRP laminate (anisotropic), and the two types of damage commonly associated with each material, cracks and delaminations, respectively.

3.1. Experimental setup

We use a cantilever beam of length 463mm, with one end attached to a shaker and the other end free to oscillate, and a slow-motion camera (FASTCAM SA3 model 120K-M2) to record the motion of the beam. A picture of such a setup can be found in Figure 5. The following materials were evaluated:

(i) Three steel beams of dimension 2.35mm × 61.5mm × 463mm, each with a machined notch 5mm wide of increasing depths (5%, 28% and 50% respectively) at a distance of 149mm (1/3 of the total length) from the free end (see Figure 6 for a schematic).

Figure 5. Picture of the cantilever beam setup, fixed end is attached to a mechanical shaker
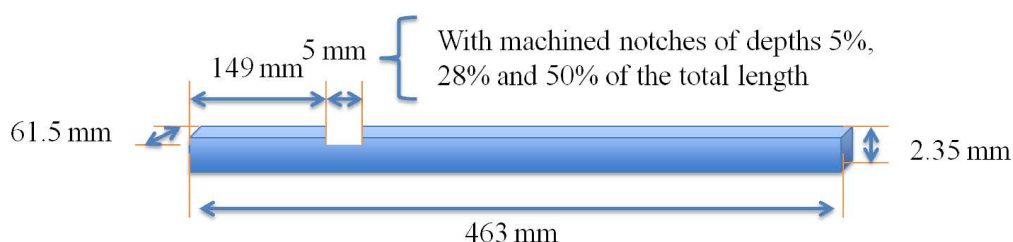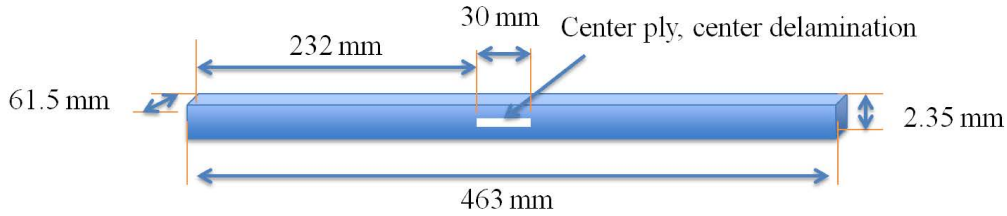

Figure 6. Schematic diagram of the three steel beams

Of these, the two higher damage levels are primarily to illustrate clearly the function of the detection method and much greater than is likely to be sustained as "damage" in a real situation. However, although 5% of 2.35mm is small in absolute terms, it remains relatively large as a percentage of whole thickness and so may not be characteristic of incipient damage.

(ii) Six $(0/90/0/90/0)_s$ CFRP laminate beams of dimension 2.35mm × 61.5mm × 463mm, made from Hexcel T700/M21; a 30mm wide delamination was manufactured in the middle layer of three beams ("centre delaminate") and between the first and second layers for the other three beams ("outer delaminate"). Each delamination type was placed at three locations: 1/3, 1/2 and 2/3 from the free end respectively (see Figure 7 for a schematic of a beam with centre delamination). The delamination was created by inserting a PTFE tape during layup. In contrast to the nature of the damage in the steel beam, it is particularly interesting to detect hidden delamination defects in composites which can develop during manufacture or in-service which can be larger than incipient cracks in metals. For example, the 30mm delamination is 10% of length and represents a relatively realistic damage feature for this kind of material.

For each of the experimental beams, 48 white circular markers were placed along its edge (Figure 2a). A slow motion camera with a spatial resolution of 1024 × 256 and frame rate of 2000 fps was used to record the motion of each test structure.

FEA models were created corresponding to each of the damaged steel and delaminated CFRP beams and used as 'ground truth' to compare with the experimental results. The FEA models were constructed using Ansys 12.1, and specified as follows:

Figure 7. Schematic diagram of one of the $(0/90/0/90/0)_s$ CFRP beams with central delamination

(i) steel beam: uses the BLC4 element type, with a Young's modulus of 208 GPa and Poisson's ratio of 0.3. (ii) CFRP beam: uses the PLANE42 element type, with E_x=136GPa, E_y=8.9GPa, E_z=8.9GPa, Poisson' Ratio of 0.35 and G_{xy} of 4.5GPa. Individual layers were created to represent the $(0/90/0/90/0)_s$ layup of the 10-ply laminate and air gaps in the model where introduced to represent the delamination. For both models, boundary conditions were applied to represent the attachment of one end of the beam to the shaker. Modal analysis was conducted to examine the beam shape at the first two modal frequencies. Nodal positions were extracted to form the modal shape of the damaged structures and 194 nodal displacements were extracted from each FEA modal shape. A cubic spline was fitted to the displaced nodal points in the same manner as the experimental beams.

The damage detection results are presented in each case through three sets of graphs. The first set demonstrate the effectiveness of the wavelet approach to detection and location in an isotropic and an anisotropic setting, by showing experimental results computed at sub-pixel accuracy. The second set shows the results computed using the FEA models. The side-by-side comparison of these two confirms earlier results of [24], and extends their findings in terms of accuracy. Accuracy is the motivation for the third set of graphs, which demonstrate the critical role played by the sub-pixel, versus the pixel-based, Hough transform, where we show that the latter generates inconclusive signals for anything except relatively severe damage.

3.2. Detection Results for Steel Beams

The graphs for the steel beams (beam length: 463mm, mode number: 2) are given in figure 9. Figures 9(a)–9(c) shows the damage severity and location captured from the video of the beams, using the sub-pixel accurate Hough transform, with damage levels of 5%, 28% and 50%, and modal frequencies of 66.5Hz, 65.9Hz and 63.2Hz, respectively. Figures 9(d)–9(f) shows the same results, but derived from the FEA model for the same damage levels. This comparison demonstrates the performance of the sub-pixel Hough transform in an experimental setting against the ideal situation represented by the FEA model. In all these graphs, the x-axis denotes the length of the beam (normalized by the total length), the y-axis represents the wavelet scale and the z-axis is the coefficient values. Figures 9(g)–9(i) use the standard (pixel accurate) Hough transform, again
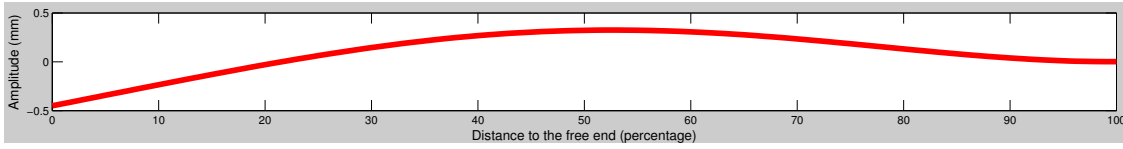
(a) An example modal shape (mode 2) of one FEA beam
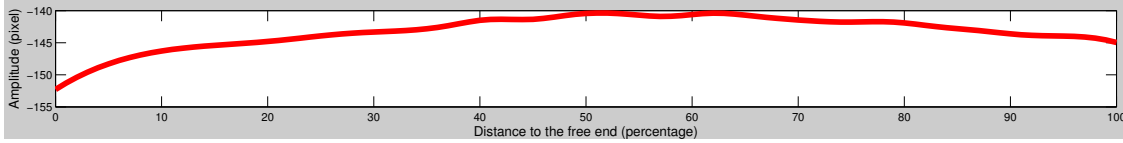
(b) An example modal shape (mode 2) of one experimental beam

Figure 8. A comparison of modal shapes acquired numerically (top) and experimentally (bottom). The right hand side is fixed to the shaker.

with damage levels of 5%, 28% and 50%. This allows comparison with both sub-pixel and FEA and demonstrates the increased accuracy achieved by means of the sub-pixel Hough transform.

Experiments were also conducted using the first modal shapes with similar results. Second modal shapes are preferred mainly because they exhibit more local bending that highlights better the damage response. Figure 8 compares numerical and experimental modal shapes. CWT coefficient plots of the three beams under its second mode of resonance are shown in figure 9(a)–9(c) using sub-pixel HT. The coefficients are plotted as height maps where larger values simply correspond to observable peaks. For 28% and 50% damage, the CWT coefficient clearly peaks in the vicinity of the machined notch, i.e., 1/3 of the total length of the beam from the free end where $x = 0$. The 5% damaged beam is less conclusive. Corresponding results from the second mode of resonance shapes from FEA are given in figures 9(d)–9(f). As can be seen, they correlate well with the results from physical experiments. It is worth noting that the magnitude of the peak of the wavelet coefficient (i.e., peaks that correspond to damage locations) appears to grow proportionally with the degree of damage (5%, 28% and 50%). Overall, because of the noise-free nature of the FEA numerical data, coefficient height maps in figure 9(d)–9(f) tend to be smoother than those from the experiments in figures 9(a)–9(c).

To demonstrate the importance of the use of sub-pixel HT, we compare results using sub-pixel HT in figure 9(a)–9(c) and standard (pixel accurate) HT in figure 9(g)–9(i). Pixel accurate HT produces inconclusive results on beams with 5% and 28% damage, where wavelet coefficient peaks are both insignificant and noisy, in contrast to the sub-pixel results that more readily identify and locate the damage. Damage is however detected on the beam with 50% damage using the standard HT, a result that confirms the conclusions of Rucka and Wilde [24] who observed a detection limit at 50% material removal.
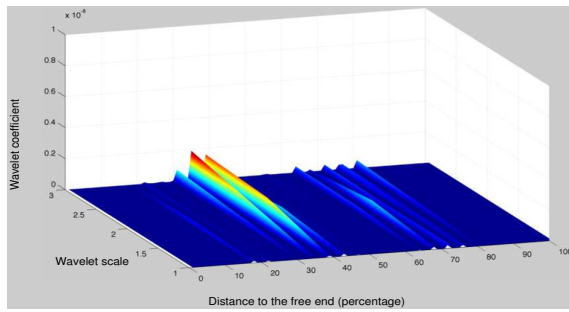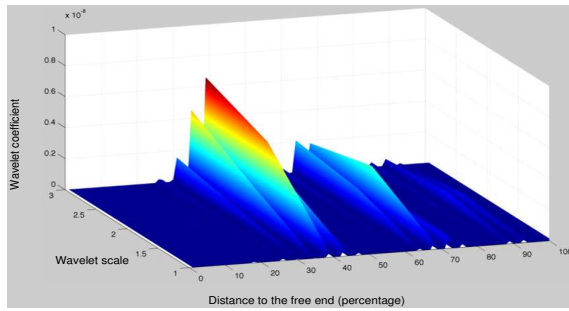
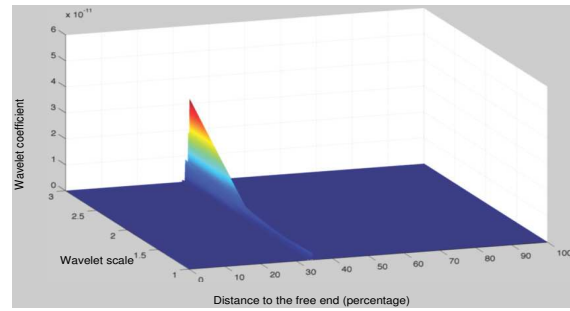(a) Steel, notch depth: 5%, sub-pixel HT
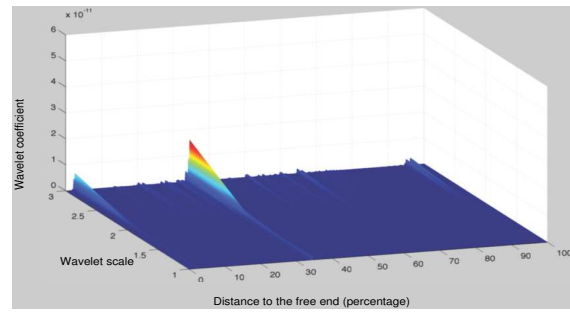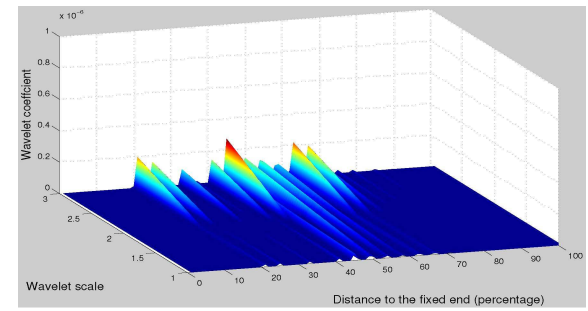
(d) Steel, notch depth: 5%, FEA
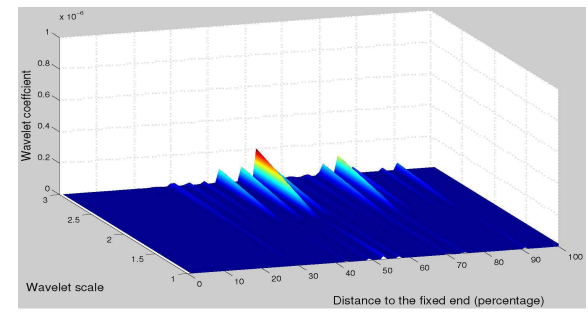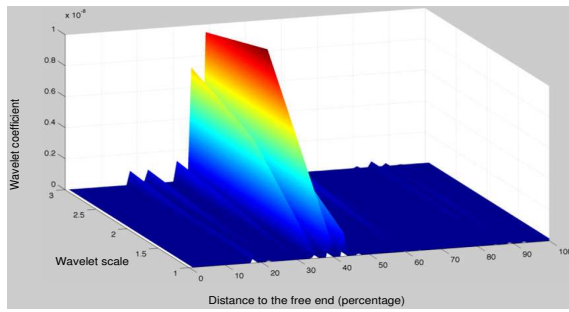
(g) Steel, notch depth: 5%, standard HT

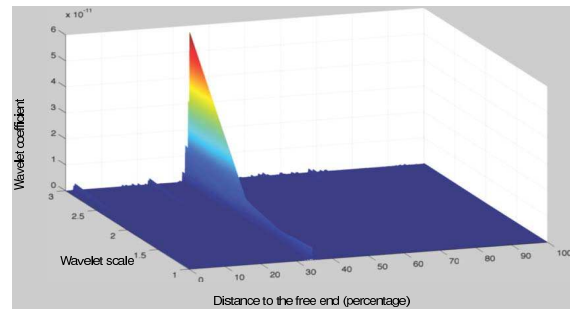(b) Steel, notch depth: 28%, sub-pixel HT
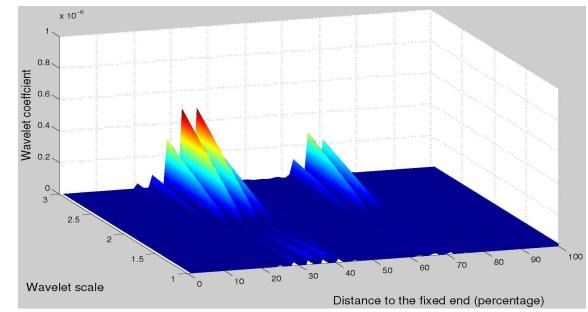
(e) Steel, notch depth: 28%, FEA

(h) Steel, notch depth: 28%, standard HT

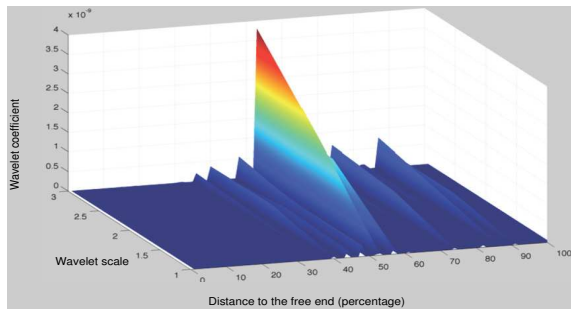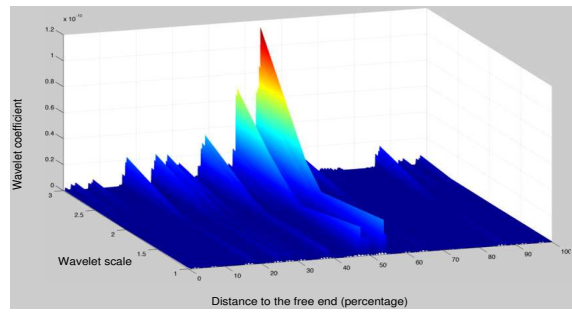(c) Steel, notch depth: 50%, sub-pixel HT

(f) Steel, notch depth: 50%, FEA
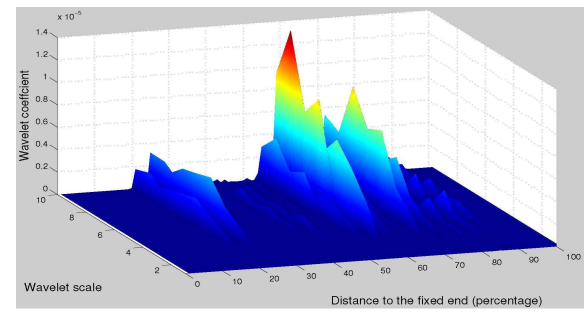
(i) Steel, notch depth: 50%, standard HT

Figure 9. Damage detection results for steel beam using sub-pixel HT 9(a)–9(c), FEA model 9(d)–9(f) and standard HT 9(g)–9(i). The axes in each case are x: wavelet scale, y: Distance to the fixed end (percentage) and z: wavelet coefficient
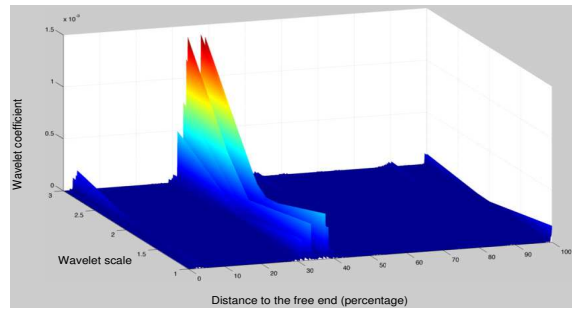
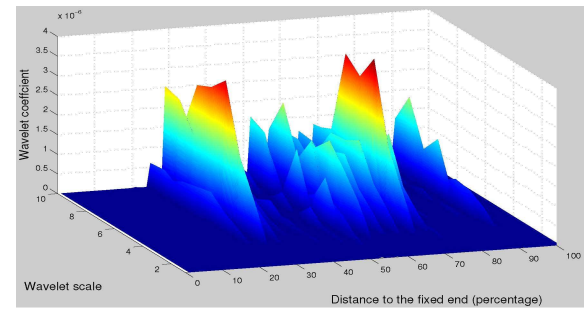(a) CFRP, centre, 1/2, sub-pixel HT

(b) CFRP, centre, 1/3, sub-pixel HT

(c) CFRP, centre, 2/3, sub-pixel HT

(d) CFRP, centre, 1/2, FEA
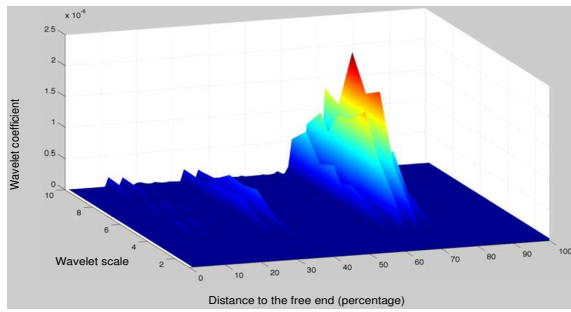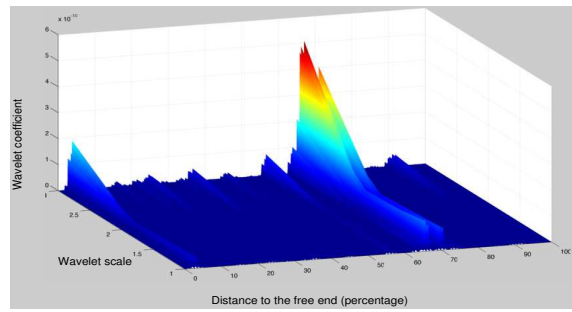
(e) CFRP, centre, 1/3, FEA

(f) CFRP, centre, 2/3, FEA

(g) CFRP, centre, 1/2, standard HT

(h) CFRP, centre, 1/3, standard HT

(i) CFRP, centre, 2/3, standard HT

Figure 10. Damage detection results for CFRP beam with centre layer delamination using sub-pixel HT 10(a)–10(c), FEA model 9(d)–9(f) and standard HT 10(g)–10(i). The axes in each case are x: wavelet scale, y: Distance to the fixed end (percentage) and z: wavelet coefficient

(a) CFRP, outer, 1/2, sub-pixel HT

(d) CFRP, outer, 1/2, FEA

(g) CFRP, outer, 1/2, standard HT

(b) CFRP, outer, 1/3, sub-pixel HT

(e) CFRP, outer, 1/3, FEA
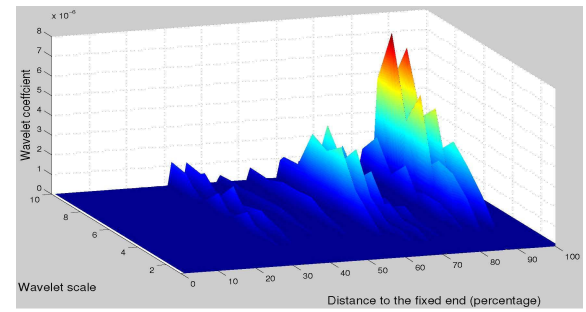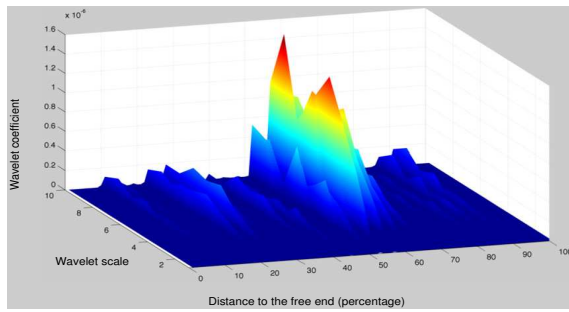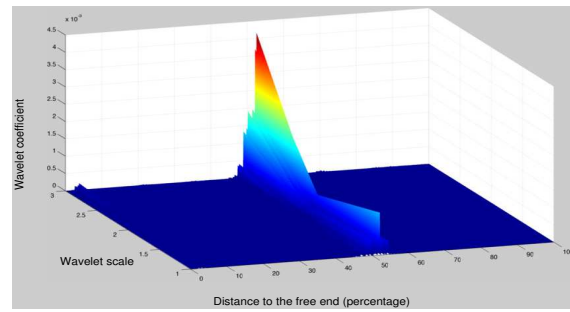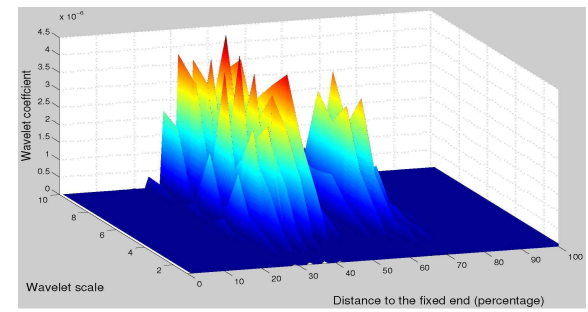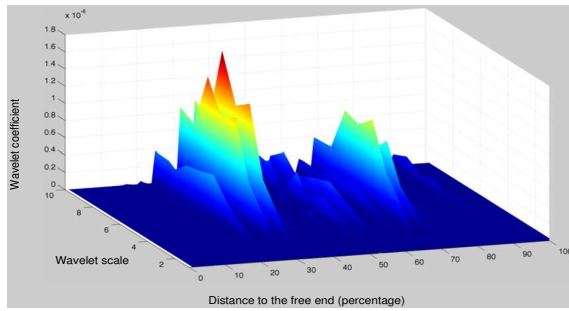
(h) CFRP, outer, 1/3, standard HT
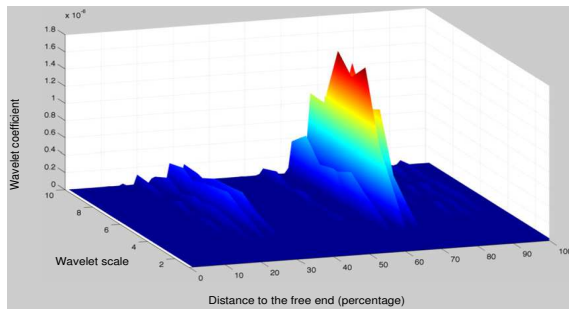
(c) CFRP, outer, 2/3, sub-pixel HT
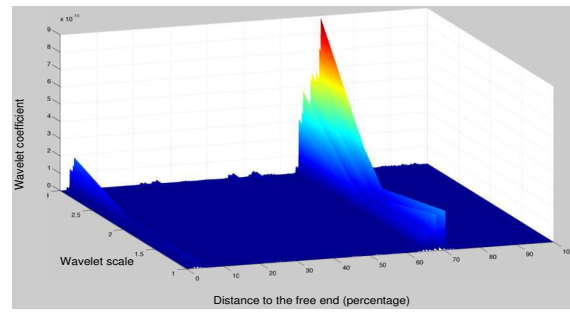
(f) CFRP, outer, 2/3, FEA

(i) CFRP, outer, 2/3, standard HT

Figure 11. Damage detection results for CFRP beam with outer layer delamination using sub-pixel HT 11(a)–11(c), FEA model 11(d)–11(f) and standard HT 11(g)–11(i). The axes in each case are x: wavelet scale, y: Distance to the fixed end (percentage) and z: wavelet coefficient
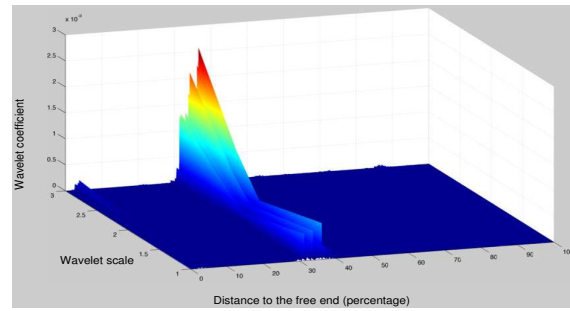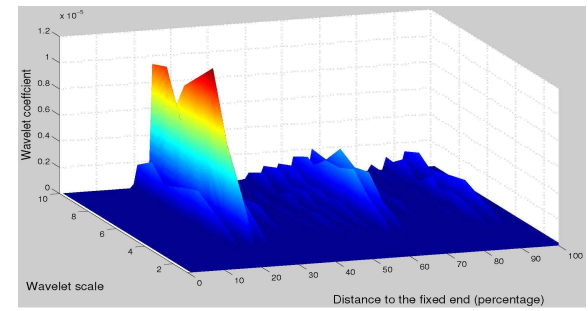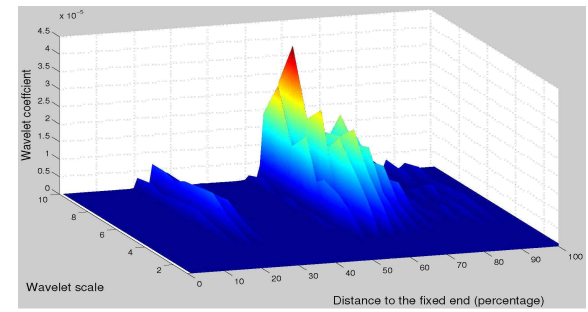
3.3. Detection Results for Composite Beams

We assessed six CFRP laminates with various delamination defects of 30mm in length as detailed in Section 3.1. Figures 10(a)–10(c) give damage detection results for three CFRP beams where the delamination was located within the middle layer at a distance of 1/2, 1/3 and 2/3 from the free-end, where $x = 0$. Figures 11(a)–11(c) show data for three further CFRP beams, where the delamination is between the first and second layer at a distance of 1/2, 1/3 and 2/3 from the free-end. The corresponding figures 10(d)–10(f) and 11(d)–11(f) give the results using the FEA model.

As can be seen in both Figures 10 and 11, in all cases, a strong peak of wavelet coefficients is observable where the delamination is located in both the experimental and finite element data. As observed for the steel beams, FEA results offer noise-free responses compared to physical beams. However, unlike the isotropic steel beams where the heights of wavelet coefficient peaks grows proportionally with the degree of the damage, the rather different nature of the damage on CFRP beams triggers some notable differences in the wavelet responses:

 (i) The response appears to contain two neighbouring peaks, rather than a single one peak observed for the steel beams, this effect is particularly apparent in Figure 10(b), which can lead to errors in damage location identification. The reason behind such a behaviour potentially lies with the nature of delamination damage where local discontinuities occur at the boundaries of the actual delamination. This also confirms experimental conclusions from recent work by Wang et. al. [13].

 (ii) Wavelet coefficients tend to be less noisy on beams with outer layer delamination damage compared to those with centre delaminations, which is also the case with the finite element data. This is best seen when comparing figure 10(b) and figure 11(b).

 (iii) Damage also tends to be more readily detected closer to the fixed end of the beam, where the structure undergoes more strain. Figures 10(b) and 10(c), and figures 11(b) and 11(c) both illustrate such an effect.

The combination of modal shape reconstruction and WT is able to detect the delaminations of the order of 30mm in these CFRP structures.

4. CONCLUSIONS

This paper presents a novel non-invasive damage detection system that utilises a camera, markers and a modal shape reconstruction algorithm based on computer vision techniques. The acquired modal shapes are used as an input into a WT-based algorithm to detect and locate damage. The system benefits from a novel sub-pixel HT extraction algorithm that is both accurate and efficient. For steel beams, notch depths of 5%, 28% and 50% were detected using sub-pixel HT and 30mm delaminations were detected in central and outer layers of a composite laminate. For future work, smaller notch depths and finer spatial resolution of damage need to be investigated, but these contain significant challenges in the form of enhancing sensitivity to lighter damage at the same

time as reducing incidence of false positives. A further set of experiments are required to explore the the sensitivity of the modal shape reconstruction process to the relative positions of damage to features of the modal shape.

Our work confirms the applicability of cameras for SHM and NDE applications when combined with modern computer vision techniques. The approach enables structural health monitoring of structures without the need for attaching accelerometers/strain gauges or employing laser positioning systems. A single camera node could potentially capture a number of markers and efficiently transmit the acquired data across a network.

The methodology could further be applied to: (i) the processing of the camera data in the temporal domain, for example, linking the markers extracted in time to enable dynamic testing of structures; (ii) quantifying the observed correlation between wavelet magnitudes at damage locations and the degree of damage; (iii) extending the algorithm to characterise more types of damage on composite materials, such as the layer of damage and not just its location.

ACKNOWLEDGMENTS

[1] E. Peter Carden and Paul Fanning. Vibration based condition monitoring: A review. *Structural Health Monitoring*, 3(4):355–377, 12 2004.

[2] M Radzieński and M Krawczuk. Experimental verification and comparison of mode shape-based damage detection methods. *Journal of Physics: Conference Series*, 181(1):012067, 2009.

[3] S.W. Doebling, C.R. Farrar, M.B. Prime, and D.W. Shevitz. Damage identification and health monitoring of structural and mechanical systems from changes in their vibration characteristics: A literature review. Technical Report LA–13070-MS, Los Alamos National Lab., 1996. DOI 10.2172/249299.

[4] Scott W. Doebling, Charles R. Farrar, and Michael B. Prime. A summary review of vibration-based damage identification methods. *THE SHOCK AND VIBRATION DIGEST*, 30:91–105, 1998.

[5] H Sohn. *A review of structural health monitoring literature: 1996-2001*, volume LA-13070-MS. Los Alamos National Laboratory report, 2004.

[6] Wei Fan and Pizhong Qiao. Vibration-based damage identification methods: A review and comparative study. *Structural Health Monitoring*, 2010.

[7] Z. Hou, M. Noori, and R. St. Amand. Wavelet-based approach for structural damage detection. *Journal of Engineering Mechanics*, 126(7):677–683, 2000.

[8] A Chukwujekwu Okafor and A Dutta. Structural damage detection in beams by wavelet transforms. *Smart Materials and Structures*, 9(6):906, 2000.

[9] M. M. Reda Taha, A. Noureldin, J. L. Lucero, and T. J. Baca. Wavelet Transform for Structural Health Monitoring: A Compendium of Uses and Features. *Structural Health Monitoring*, 5(3):267–295, 2006.

[10] Gilbert-Rainer Gillich, Zeno-Iosif Praisach, and Claudiu Mirel Iavornic. Reliable method to detect and assess damages in beams based on frequency changes. In *Proceedings of the ASME 2012 International Design Engineering Technical Conferences, Computers and Information in Engineering Conference IDETC/CIE 2012*, pages 109–120, Chicago, Illinois, USA, August 2012.

[11] S T Quek, Q Wang, L Zhang, and K H Ong. Practical issues in the detection of damage in beams using wavelets. *Smart Materials and Structures*, 10(5):1009, 2001.

[12] S. Patsias and W. J. Staszewskiy. Damage Detection Using Optical Measurements and Wavelets. *Structural Health Monitoring*, 1(1):5–22, 2002.

[13] Quan Wang and Nan Wu. Detecting the delamination location of a beam with a wavelet transform: an experimental study. *Smart Materials and Structures*, 20(1):012002, 2011.

[14] Stas Goferman, Lihi Zelnik-Manor, and Ayellet Tal. Context-aware saliency detection. In *CVPR*, pages 2376–2383. IEEE, 2010.

[15] Yi-Zhe Song, Pablo Arbelaez, Peter Hall, Chuan Li, and Anupriya Balikai. Finding semantic structures in image hierarchies using Laplacian graph energy. In Kostas Daniilidis, Petros Maragos, and Nikos Paragios, editors, *Computer Vision – ECCV 2010*, volume 6314 of *Lecture Notes in Computer Science*, pages 694–707. Springer Berlin / Heidelberg, 2010.

[16] Duy-Nguyen Ta, Wei-Chao Chen, Natasha Gelfand, and Kari Pulli. SURFTrac: Efficient tracking and continuous object recognition using local feature descriptors. In *International Conference on Computer Vision and Pattern Recognition*, pages 2937–2944, 2009.

[17] Jing Shi, Xiangjun Xu, Jialai Wang, and Gong Li. Beam damage detection using computer vision technology. *Nondestructive Testing and Evaluation*, 9(1):1477–2671, 2009.

[18] Richard O. Duda and Peter E. Hart. Use of the Hough transformation to detect lines and curves in pictures. *Commun. ACM*, 15:11–15, January 1972.

[19] Leandro A. F. Fernandes and Manuel M. Oliveira. Real-time line detection through an improved Hough transform voting scheme. *Pattern Recogn.*, 41:299–314, January 2008.

[20] David G. Lowe. Distinctive image features from scale-invariant keypoints. *International Journal of Computer Vision*, 60(2):91–110, 2004.

[21] M. Rucka and K. Wilde. Application of continuous wavelet transform in vibration based damage detection method for beams and plates. *Journal of Sound and Vibration*, 297(3-5):536 – 550,

2006.

[22] I. Daubechies, S.G. Mallat, and A.S. Willsky. Special issue on wavelet transformations and multiresolution signal analysis. *IEEE Transactions on Information Theory*, 38(2):529–532, March 1992.

[23] Stephane Mallat. *A Wavelet Tour of Signal Processing, Third Edition: The Sparse Way.* Academic Press, 3rd edition, 2008.

[24] M. Rucka and K. Wilde. Crack identification using wavelets on experimental static deflectionprofiles. *Engineering Structures*, 28(2):279 – 288, 2006.